

## Article

# High-Pressure Experimental and DFT Structural Studies of Aurichalcite Mineral

David Santamaría-Pérez <sup>1,\*</sup>, Raquel Chuliá-Jordán <sup>2</sup>, Alberto Otero-de-la-Roza <sup>3</sup>, Robert Oliva <sup>4</sup>  
and Catalin Popescu <sup>5</sup>

- <sup>1</sup> Departamento de Física Aplicada-ICMUV, MALTA Consolider Team, Universitat de Valencia, 46100 Valencia, Spain
- <sup>2</sup> Departamento de Didáctica de las Ciencias Experimentales y Sociales, Universitat de Valencia, 46022 Valencia, Spain
- <sup>3</sup> Departamento de Química Física y Analítica, Facultad de Química, Universidad de Oviedo, MALTA Consolider Team, 33006 Oviedo, Spain
- <sup>4</sup> GEO3BCN—Geosciences Barcelona, Consejo Superior de Investigaciones Científicas (CSIC), 08028 Barcelona, Spain
- <sup>5</sup> CELLS-ALBA Synchrotron Light Facility, Cerdanyola del Vallés, 08290 Barcelona, Spain
- \* Correspondence: david.santamaria@uv.es

**Abstract:** We report on high-pressure angle-dispersive synchrotron X-ray diffraction data of a natural  $\text{Zn}_{3.78(2)}\text{Cu}_{1.22(2)}(\text{CO}_3)_2(\text{OH})_6$  aurichalcite mineral up to 7.6 GPa and ab initio total energy calculations of the aurichalcite structure with three different Zn-Cu stoichiometries (Zn:Cu ratios = 10:0, 8:2 and 6:4). A monoclinic-to-triclinic displacive second-order phase transition was found experimentally at 3 GPa. The experimental bulk modulus of the initial  $P2_1/m$  aurichalcite is  $B_0 = 66(2)$  GPa, with a first-pressure derivative of  $B_0' = 9(2)$ . A comparison with other basic copper and zinc carbonates shows that this  $B_0$  value is considerably larger than those of malachite and azurite. This relative incompressibility occurs despite the fact that aurichalcite features a layered structure due to the number of directed hydrogen bonds between carbonate groups and the cation-centered oxygen polyhedra forming complex sheets. The existence of different bond types and polyhedral compressibilities entails a certain anisotropic compression, with axial compressibilities  $\kappa_{a0} = 3.79(5) \cdot 10^{-3} \text{ GPa}^{-1}$ ,  $\kappa_{b0} = 5.44(9) \cdot 10^{-3} \text{ GPa}^{-1}$  and  $\kappa_{c0} = 4.61(9) \cdot 10^{-3} \text{ GPa}^{-1}$ . Additional density-functional theory calculations on the  $C2/m$  hydrozincite-type structure with different Zn:Cu compositional ratios shows that the aurichalcite structure is energetically more stable than the hydrozincite one for compositions of Zn:Cu = 10:0, 8:2 and 6:4 at room pressure. The pure Zn aurichalcite phase, however, was predicted to transform into hydrozincite at 18 GPa, which suggests that the experimentally observed hydrozincite structure is a metastable phase.

**Keywords:** aurichalcite mineral; basic carbonate; high-pressure; phase transition; structure; hydrozincite; DFT calculations



**Citation:** Santamaría-Pérez, D.; Chuliá-Jordán, R.; Otero-de-la-Roza, A.; Oliva, R.; Popescu, C. High-Pressure Experimental and DFT Structural Studies of Aurichalcite Mineral. *Minerals* **2023**, *13*, 619. <https://doi.org/10.3390/min13050619>

Academic Editors: Daniel Hummer and Lidong Dai

Received: 3 March 2023

Revised: 15 April 2023

Accepted: 26 April 2023

Published: 28 April 2023



**Copyright:** © 2023 by the authors. Licensee MDPI, Basel, Switzerland. This article is an open access article distributed under the terms and conditions of the Creative Commons Attribution (CC BY) license (<https://creativecommons.org/licenses/by/4.0/>).

## 1. Introduction

Carbonate minerals are the most abundant carbon phases on the Earth's surface. In the subduction processes, carbonates enter into the Earth's mantle and are progressively subjected to increasing pressures and temperatures as the subduction slab sinks [1]. Consequently, the determination of the influence of these thermodynamic parameters on the stability and structural behavior of carbonates, together with the interaction of these minerals with different compositional environments, is key for geophysics. Nowadays, it is possible to recreate high-pressure (HP) and high-temperature (HT) conditions in the laboratory, and the sample can be characterized in situ by a battery of spectroscopic and diffraction techniques. Thus, numerous laboratory structural studies of simple and double carbonates at HP-HT have been reported in the last two

decades [2–14]. The investigation of the HP-HT structural behavior of carbonate minerals bearing additional anion groups such as  $[\text{PO}_4]^{3-}$  in phosphate-carbonates [15],  $[\text{SiO}_4]^{4-}$  in silicate-carbonates [16–18] or  $[\text{OH}]^-$  in basic carbonates [19–21] is, however, rather limited. In particular, the understanding of the effect of hydroxyl groups on the HP properties of carbonates has direct implications in geophysics, as  $[\text{OH}]^-$  released from hydrous minerals impacts decarbonation, dissolution and phase relations of carbonate minerals [22]. Compounds of the system  $[\text{CO}_3]$ - $[\text{OH}]$  could provide insight into the synergistic relationship between deep carbon and water cycles.

Aurichalcite  $(\text{Zn,Cu})_5(\text{CO}_3)_2(\text{OH})_6$ , in which carbonate and hydroxyl groups coexist, is a naturally-occurring mineral commonly found in association with hemimorphite  $\text{Zn}_4(\text{Si}_2\text{O}_7)(\text{OH})_2 \cdot \text{H}_2\text{O}$  and other basic carbonates such as hydrozincite  $\text{Zn}_5(\text{CO}_3)_2(\text{OH})_6$ , rosasite  $(\text{Zn,Cu})_2(\text{CO}_3)(\text{OH})_2$ , malachite  $\text{Cu}_2(\text{CO}_3)(\text{OH})_2$  or azurite  $\text{Cu}_3(\text{CO}_3)_2(\text{OH})_2$  in oxidized zones of zinc and copper deposits. The Zn:Cu ratio in natural aurichalcite samples is known to vary between 5:1 zinc-rich composition and 4:5 [23]. Aurichalcite is also important as a synthetically produced intermediate in the preparation of copper/zinc oxide catalysts for a variety of industrial hydrogenation processes, such as methanol production [24,25]. It is considered that the aurichalcite phase in the precursor plays a key role in improving the physicochemical properties and activities of the final catalysts [25]. The crystal structure of this mineral was first determined by synchrotron single-crystal X-ray diffraction (XRD) in 1994. At room conditions, aurichalcite is monoclinic, space group  $P2_1/m$ , with lattice parameters  $a = 13.82(2) \text{ \AA}$ ,  $b = 6.419(3) \text{ \AA}$ ,  $c = 5.29(3) \text{ \AA}$ ,  $\beta = 101.04(2)^\circ$  ( $V = 461(3) \text{ \AA}^3$ ,  $Z = 2$ ) for the chemical composition  $\text{Zn}_3\text{Cu}_2(\text{CO}_3)_2(\text{OH})_6$  [24]. The crystal structure of an aurichalcite specimen with a different composition,  $\text{Zn}_{2.3}\text{Cu}_{2.7}(\text{CO}_3)_2(\text{OH})_6$ , was later refined [23] with comparable unit-cell parameters. The structure consists of complex layers of cation-centered polyhedra in which the Zn and Cu atoms are in four coordination environments: two octahedral sites with different distortion, a trigonal bipyramidal site and a tetrahedral site (described in detail later). These layers are held together by hydrogen bonds. The Zn and Cu ordering in aurichalcite samples was only postulated from XRD measurements due to the fact that scattering factors of Cu and Zn are very similar. X-ray absorption spectroscopy measurements confirm that copper might be distributed across more than one metal site [26]. However, Cu atoms preferentially occupy Jahn–Teller elongated octahedral and trigonal bipyramidal sites, with Zn atoms occupying the more regular octahedral and tetrahedral sites. Interestingly, the Zn end member  $\text{Zn}_5(\text{CO}_3)_2(\text{OH})_6$ , named hydrozincite, is reported to have a different but intimately related structure, with similar unit-cell dimensions as aurichalcite but described in the monoclinic space group  $C2/m$  [27]. Moreover, DFT calculations indicate that the hydrozincite-type structure with composition  $\text{Zn}_3\text{Cu}_2(\text{CO}_3)_2(\text{OH})_6$  is thermodynamically the most stable [28]. These studies evidence the complex chemistry of this system. Several other groups have characterized aurichalcite spectroscopically [29,30] and studied its thermal stability [31].

In this work, we conducted high-pressure synchrotron XRD experiments on a naturally occurring aurichalcite  $\text{Zn}_{3.78(2)}\text{Cu}_{1.22(2)}(\text{CO}_3)_2(\text{OH})_6$  mineral and first-principles calculations on three different Zn:Cu stoichiometries to study the structural behavior and the evolution of the atomic interactions upon compression.

## 2. Materials and Methods

### 2.1. Experimental Details

A naturally occurring aurichalcite mineral specimen from the Gelbe Birke Mine, Beierfeld, Erzgebirge (Saxony, Germany) was provided by Gunnar Färber Mineralien (see photograph in the inset of Figure 1). A light blue powder was carefully isolated, crushed with a mortar and pestle and characterized at room conditions by means of energy-dispersive X-ray spectroscopy (EDX, Hitachi S4800 scanning electron microscope) and XRD. Quantitative chemical analyses indicate that the  $\text{Zn}_{3.78(2)}\text{Cu}_{1.22(2)}(\text{CO}_3)_2(\text{OH})_6$  chemical composition is quite uniform through the sample. From XRD measurements, we obtained the lattice parameters of aurichalcite:  $a = 13.809(7) \text{ \AA}$ ,  $b = 6.412(2) \text{ \AA}$ ,  $c = 5.315(3) \text{ \AA}$ ,

$\beta = 100.74(5)^\circ$  ( $V = 462.3(3) \text{ \AA}^3$ ), which are in good agreement with those previously reported in the literature [23,24]. Unfortunately, the sample is not perfectly homogeneous and does not correspond to a randomly oriented powder. Therefore, powder diffraction data present intensities that could not be used for structural Rietveld refinements, but only for unit-cell indexations and profile Le Bail refinements (see Figure 1).

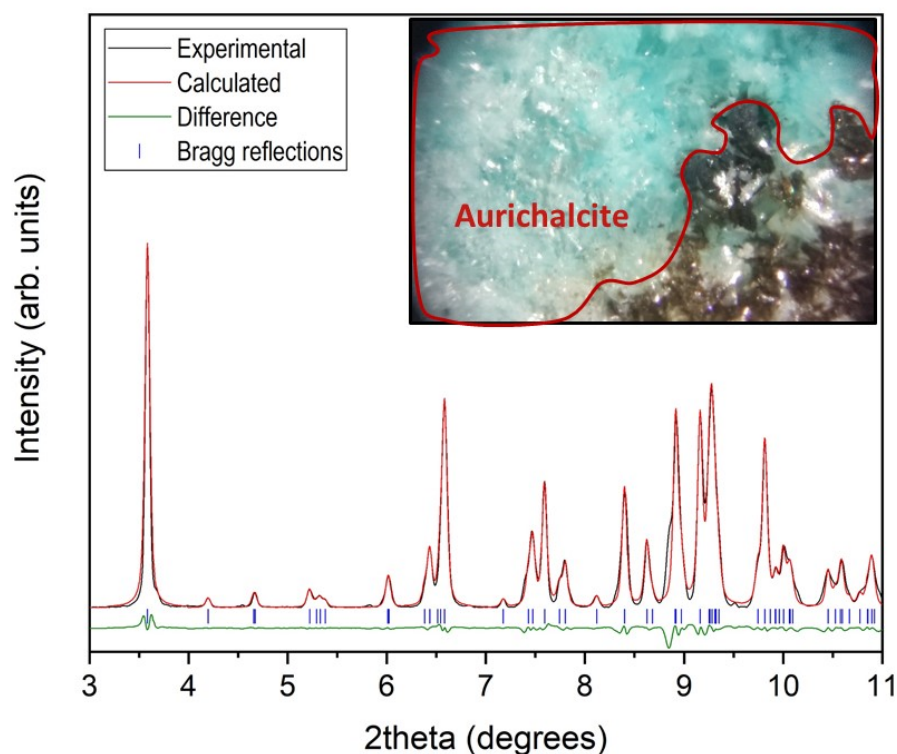


**Figure 1.** Observed, calculated and difference XRD patterns for  $\text{Zn}_{3.78(2)}\text{Cu}_{1.22(2)}(\text{CO}_3)_2(\text{OH})_6$  aurichalcite at room conditions. Vertical marks indicate Bragg reflections. Light blue aurichalcite crystals in our naturally occurring specimen (inset).

High-pressure angle-dispersive XRD experiments were conducted at room temperature at the MSPD beamline of the ALBA synchrotron source with an incident monochromatic wavelength of  $0.4246 \text{ \AA}$  focused to  $30 \times 30 \mu\text{m}^2$  [32]. Measurements up to 7.6 GPa were performed in a membrane diamond-anvil cell with diamond culets of  $500 \mu\text{m}$ . Aurichalcite powder was loaded in a  $250 \mu\text{m}$  diameter hole of an inconel gasket preindented to a thickness of about  $50 \mu\text{m}$ . Silicone oil was used as the pressure-transmitting medium [33], and the pressure was determined using the equation of state (EOS) of copper [34], which was included in the pressure chamber. Detector calibration, correction of distortion and integration to conventional  $2\theta$ -intensity data were carried out with the Dioptas software [35]. The indexing and refinement of the powder patterns were performed using the Unitcell [36], Fullprof [37] and Powdercell [38] program packages.

## 2.2. Computational Details

We considered two phases corresponding to the experimental structures of aurichalcite and hydrozincite. In the latter, the hydrogen positions were not available from the experimental diffraction data, and we placed them manually based on the oxygen distances prior to the geometry relaxation. In addition, for each of the two phases, we considered three compositions: pure Zn, Zn:Cu ratio = 6:4, and the Zn:Cu ratio that most resembles the experimentally determined atomic ratio. Since there are ten atoms of Cu plus Zn in the unit-cell in both phases, we opted for an 8:2 ratio of Zn:Cu, which adequately fits our measured value while maintaining the relative simplicity of the DFT calculations.

Density functional theory (DFT) calculations were performed using the projector-augmented wave (PAW) method [39] implemented in Quantum ESPRESSO [40], version 6.5. The B86bPBE [41,42] functional was used in combination with the exchange-hole dipole moment (XDM) dispersion model [43–45]. Even though DFT has difficulties modeling electronic excitation properties such as band gaps [46], it has been tremendously successful in describing ground-state properties such as the relative stabilities of polymorphs under pressure. The PAW datasets came from the pslibrary [47] and had 1 (H), 4 (C), 6 (O), 11 (Cu) and 12 (Zn) valence electrons. We used cutoffs of 80 Ry for the orbital and 800 Ry for the electron density expansions. A uniform k-point grid of dimensions  $2 \times 3 \times 4$  was used for both phases, ensuring a convergence of around 0.1 mRy in the energy and 0.01 GPa in the calculated pressure.

In this system, the Cu atom has a  $d^9$  valence electronic structure, and therefore, the calculations were run with spin-polarization. Cold smearing [48] was used with a smearing parameter of 0.01 Ry. Cursory single-point calculations at the aurichalcite experimental geometry of the Zn:Cu 8:2 composition revealed that the ferromagnetic (FM) and antiferromagnetic (AFM) orderings are very similar in energy, with the FM order being slightly favored. Because of this, and also because the calculations are simpler, the FM order was used in all calculations.

In the case of the Zn:Cu 8:2 composition, we examined the question of how to distribute the Zn and Cu atoms over the 10 available positions. Since the Cu(I) is likely to deform the coordinating oxygen atoms in its vicinity, we relaxed the geometries of the 45 possible arrangements of 8 Zn and 2 Cu atoms over the 10 positions in the unit-cell for the aurichalcite and hydrozincite phases. In the aurichalcite case, the Cu atoms prefer occupying the 4f Wyckoff positions of the  $P2_1/m$  space group ( $1/4,0,z$ ) forming atomic chains along the  $b$  axis. We use the most stable zero-pressure atomic configuration of aurichalcite and hydrozincite to calculate the equation of state. Tables S1 and S2 with the relative energies, volumes and space groups of all atomic arrangements for the aurichalcite and hydrozincite phases are shown in the Supporting Information. Using the procedure described below, we calculated the equation of state of two other arrangements per phase, in addition to the minimum-energy one. It is shown in the Supporting Information that, although there are minor differences in the energy–volume and enthalpy–pressure curves depending on atomic configuration (see Figures S1 and S2), the relative stability of the aurichalcite/hydrozincite phases is captured by the minimum-energy atomic arrangement. Therefore, we will discuss only the latter in the rest of the manuscript.

Geometry relaxations were carried out at constant zero and 50 GPa pressures of the aurichalcite and hydrozincite phases with pure Zn and Zn:Cu 8:2 and 6:4 compositions. In all geometry relaxations, energy and force cutoffs of  $10^{-5}$  Ry and  $10^{-4}$  Ry/bohr were used, respectively. The resulting equilibrium geometries were then used to build a uniform volume grid with 41 points spanning the corresponding pressure range. Constant volume geometry relaxations were carried out at each of these 41 points for every phase and composition, and the resulting energy–volume curves were fitted with a polynomial strain average using gibbs2 [49,50] to find the relative stability of each phase.

### 3. Results and Discussion

The indexation of the XRD pattern at room conditions yields lattice parameters consistent with those of the previously published aurichalcite structure, the peak intensities are in good agreement with the reported structure despite the non-homogeneous particle-size sample, and our DFT calculations confirm that the aurichalcite structure is thermodynamically stable. The crystal structure of aurichalcite at room conditions consists of complex sheets perpendicular to the (100) direction, which are interconnected by hydrogen bonds (see Figure 2). Each of these sheets is composed of double layers of close-packed O atoms that contain metal atoms in two slightly different octahedral coordination environments. According to previous single-crystal XRD results [23], four Zn/Cu atoms per unit-cell are located in tetragonally Jahn–Teller distorted octahedral sites with four short metal–oxygen



distances ( $2 \times 1.98 \text{ \AA} + 2 \times 2.01 \text{ \AA}$ ) and two long distances ( $2 \times 2.33 \text{ \AA}$ ), whereas two Zn/Cu atoms per unit-cell are centering other octahedra with a smaller range of metal-oxygen distances ( $1.98\text{--}2.21 \text{ \AA}$ ). Diffraction and especially spectroscopic results suggest that the Cu atoms preferentially occupy the first of these octahedral types, which are connected by common edges forming chains along the *b* axis. These distorted Jahn–Teller octahedra share other edge with more regular octahedra, and they are corner-linked to both metal-centered O tetrahedra and trigonal bipyramids situated at opposite sides of the octahedral-based layer. The sides of these complex sheets where the tetrahedra are located face each other and are connected by carbonate groups and hydrogen bonds. The sides of these complex sheets where the trigonal bipyramids are located face each other and are only connected by weak hydrogen bonds.

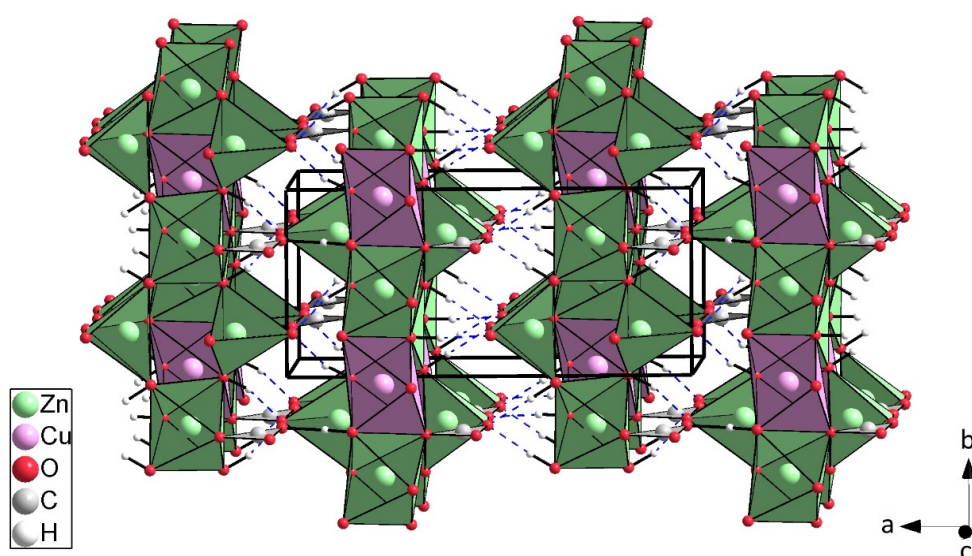


**Figure 2.** The structure of DFT-calculated  $\text{Zn}_4\text{Cu}(\text{CO}_3)_2(\text{OH})_6$  aurichalcite projected roughly along the (001) direction. Green, magenta, red, gray and white spheres correspond to the Zn, Cu, O, C and H atoms, respectively. Cation-centered oxygen polyhedra are depicted. Hydrogen bonds are represented as dashed blue lines.

Diffraction patterns measured at different pressures are shown in Figure 3. Upon compression, the diffraction peaks shift to higher  $2\theta$  angles as expected, but there are no significant variations in relative diffraction intensities of the XRD peaks and no appearance of new diffraction peaks up to the maximum pressure reached in this study, 7.6 GPa. Up to 3 GPa, the XRD patterns could be indexed in the monoclinic cell, similar to that at room pressure. The experimental unit-cell parameters and volumes of the monoclinic  $P2_1/m \text{ Zn}_{3.78(2)}\text{Cu}_{1.22(2)}(\text{CO}_3)_2(\text{OH})_6$  aurichalcite at different pressures are collected in Table 1. Above 3 GPa, the indexation process suggests a triclinic unit-cell, a fact that agrees with a better LeBail fit using a slightly distorted *P*-1 structure (see Figure S3 of the Supplementary Information). The experimental unit-cell parameters and volumes of the triclinic *P*-1  $\text{Zn}_{3.78(2)}\text{Cu}_{1.22(2)}(\text{CO}_3)_2(\text{OH})_6$  aurichalcite at different pressures are collected in Table 2. Remarkably, a structure with comparable lattice dimensions was predicted by our DFT calculations for a Zn:Cu 8:2 composition. The DFT-calculated lattice parameters and atomic coordinates at 2.76 GPa can be found within a cif file in the Supplementary Information. Above 6 GPa, the XRD patterns could not be successfully indexed due to their deterioration under non-hydrostatic compression.

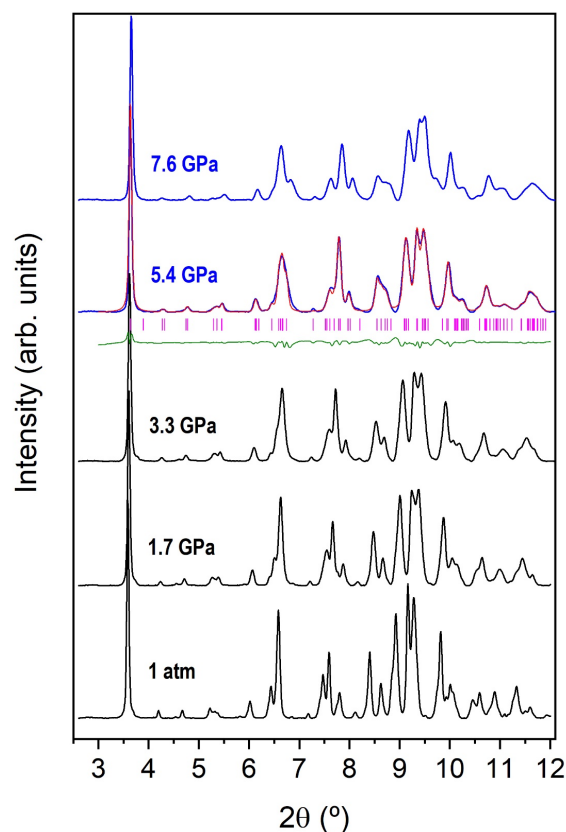


**Figure 3.** Room-temperature angle-dispersive XRD data of  $\text{Zn}_{3.78(2)}\text{Cu}_{1.22(2)}(\text{CO}_3)_2(\text{OH})_6$  aurichalcite at different pressures. Background was subtracted. The XRD patterns of the initial  $P2_1/m$  and the high-pressure  $P-1$  phases are represented as black and blue solid lines, respectively. Calculated and difference XRD profiles for the  $P-1$  phase at 5.4 GPa and room temperature are depicted as red and green lines. Magenta vertical marks indicate Bragg reflections at these conditions.

**Table 1.** Lattice parameters and unit-cell volumes of the initial  $P2_1/m$   $\text{Zn}_{3.78(2)}\text{Cu}_{1.22(2)}(\text{CO}_3)_2(\text{OH})_6$  aurichalcite phase at different pressures and room temperature.

Pressure (GPa)	<i>a</i> Axis (Å)	<i>b</i> Axis (Å)	<i>c</i> Axis (Å)	$\beta$ (°)	Volume (Å <sup>3</sup> )
0.00	13.809(7)	6.412(2)	5.313(3)	100.70(5)	462.3(3)
0.00	13.806(7)	6.410(2)	5.315(3)	100.65(5)	462.3(3)
0.10	13.806(7)	6.413(2)	5.315(3)	100.68(5)	462.5(3)
0.15	13.800(7)	6.408(2)	5.310(3)	100.64(5)	461.6(3)
0.25	13.794(7)	6.401(2)	5.309(3)	100.60(5)	460.8(3)
0.40	13.787(7)	6.399(2)	5.304(3)	100.58(5)	460.1(3)
0.6	13.774(7)	6.388(2)	5.300(3)	100.52(5)	458.5(3)
0.75	13.767(7)	6.386(2)	5.293(3)	100.50(5)	457.7(3)
0.9	13.759(7)	6.379(2)	5.293(3)	100.45(5)	456.9(3)
1.05	13.750(7)	6.374(2)	5.286(3)	100.42(5)	455.8(3)
1.25	13.741(7)	6.368(2)	5.281(3)	100.39(5)	454.7(3)
1.35	13.731(7)	6.361(2)	5.280(3)	100.33(5)	453.7(3)
1.55	13.721(7)	6.356(2)	5.273(3)	100.31(5)	452.6(3)
1.70	13.715(7)	6.350(2)	5.272(3)	100.26(5)	451.8(3)
1.90	13.706(7)	6.344(2)	5.266(3)	100.23(5)	450.7(3)
2.1	13.698(7)	6.337(2)	5.262(3)	100.18(5)	449.6(3)
2.35	13.685(7)	6.331(2)	5.258(3)	100.14(5)	448.5(3)
2.60	13.674(7)	6.323(2)	5.251(3)	100.06(5)	447.1(3)
2.80	13.663(7)	6.316(2)	5.248(3)	100.04(5)	446.0(3)

**Table 2.** Lattice parameters of the high-pressure  $P$ -1  $\text{Zn}_{3.78(2)}\text{Cu}_{1.22(2)}(\text{CO}_3)_2(\text{OH})_6$  aurichalcite phase at different pressures and room temperature.

Pressure (GPa)	<i>a</i> Axis (Å)	<i>b</i> Axis (Å)	<i>c</i> Axis (Å)	$\alpha$ (°)	$\beta$ (°)	$\gamma$ (°)	Volume (Å <sup>3</sup> )
3.3	13.663(8)	6.307(3)	5.244(4)	90.28(7)	100.05(6)	89.52(8)	444.9(5)
3.5	13.653(8)	6.298(3)	5.240(4)	90.30(7)	100.03(6)	89.44(8)	443.6(5)
4.0	13.638(9)	6.287(3)	5.232(4)	90.30(7)	100.00(6)	89.37(8)	441.7(5)
4.6	13.622(9)	6.275(3)	5.224(4)	90.30(7)	99.97(7)	89.31(8)	439.8(5)
4.9	13.607(9)	6.266(3)	5.219(4)	90.29(7)	99.93(7)	89.25(8)	438.3(5)
5.4	13.599(9)	6.258(3)	5.214(4)	90.28(7)	99.94(7)	89.20(8)	437.0(5)
6.0	13.583(10)	6.246(3)	5.206(5)	90.25(7)	99.96(7)	89.09(9)	435.0(6)

The variation in volume with pressure is represented in Figure 4. No volume discontinuity occurs at the phase transition, which points to a displacive second-order phase transformation. Importantly, despite the fact that the silicone oil used as a pressure-transmitting medium is considered quasi-hydrostatic up to 12 GPa, the pressure onset of the phase transition coincides with the pressure at which gradients were reported to appear in this pressure medium [33,51]. Therefore, a possible explanation would be the formation of a metastable  $P$ -1 phase as a consequence of the appearance of internal stresses in the sample due to non-hydrostatic conditions. A Murnaghan equation of state (EOS) was fitted to the  $P$ - $V$  data in the hydrostatic range (below 3 GPa), leaving the zero-pressure volume ( $V_0$ ), the bulk modulus ( $B_0$ ) and its first derivative with respect to pressure ( $B'_0$ ) to vary freely. The best-fit values were  $V_0 = 462.52(12)$  Å<sup>3</sup>,  $B_0 = 66(2)$  GPa and  $B'_0 = 9(2)$  GPa. The high  $B'_0$  value indicates that the bulk modulus  $B_0$  increases considerably with increasing pressure, and it was proposed in the literature to be likely correlated to the evolution of metal coordination polyhedra, as a consequence of the electronic change with increasing pressure in the basic carbonate malachite  $\text{Cu}_2\text{CO}_3(\text{OH})_2$  [19]. These experimental results are in relatively good agreement with DFT calculations that predict  $V_0 = 455.47(3)$  Å<sup>3</sup>,  $B_0 = 84.6(7)$  GPa and  $B'_0 = 4.5(3)$  GPa (see Figure 4). A comparison with other basic copper and zinc carbonates shows that the aurichalcite  $B_0$  value is considerably larger than those of  $\text{Cu}_2\text{CO}_3(\text{OH})_2$  malachite ( $B_0 = 48(4)$  GPa,  $B'_0 = 7.0(16)$ ) and  $\text{Cu}_3(\text{CO}_3)_2(\text{OH})_2$  azurite ( $B_0 = 40(2)$  GPa,  $B'_0 = 5.5(6)$ ). This difference in compressibility occurs despite the fact that octahedral ( $\text{CuO}_6$ ) and trigonal planar ( $\text{CO}_3$ ) groups of malachite and azurite are interconnected, forming a three-dimensional framework, and aurichalcite is a layered structure. This result evidences the importance of hydrogen bonds in aurichalcite, which strengthen the structure by means of three hydrogen bond connections between the octahedral framework and each carbonate group. The structure's compressibility is, for instance, similar to the rosasite-type high-pressure polymorph of  $\text{Cu}_2\text{CO}_3(\text{OH})_2$  ( $B_0 = 80(2)$  GPa,  $B'_0$  fixed to 4) [19].

An interesting observation concerns the calculated values of the unit-cell volume and the bulk modulus for a compositionally variable Zn:Cu aurichalcite system. Figure 4 shows that the larger the Zn content, the larger the unit-cell volume. This is consistent with the smaller radius of  $\text{Cu}^{2+}$  cations. Our DFT calculations for aurichalcite structures with Zn:Cu ratios of 10:0 and 6:4 were described with the monoclinic  $P2_1/m$ , whereas for the 8:2 ratio with Cu atoms in half of the tetragonally distorted octahedral sites, the mirror planes and the  $2_1$  screw axes disappear (S.G.  $P$ -1). Our pure Zn and Zn:Cu = 6:4 results show that aurichalcite becomes slightly more incompressible with increasing Cu content.

The experimentally obtained evolution of the aurichalcite unit-cell parameters at high pressure was collected in Tables 1 and 2, and the relative compressibilities of its axes are plotted in Figure 5. The axial compressibilities, defined as  $\kappa = -1/x(\partial x/\partial P)$  (where  $x = a, b, c$ ), that were estimated from our experimental  $P2_1/m$  data are  $\kappa_{a0} = 3.79(5) \cdot 10^{-3}$  GPa<sup>-1</sup>,  $\kappa_{b0} = 5.44(9) \cdot 10^{-3}$  GPa<sup>-1</sup> and  $\kappa_{c0} = 4.61(9) \cdot 10^{-3}$  GPa<sup>-1</sup>, which evidence the anisotropy in this compound. Figure 5 clearly shows that the less compressible axis is the  $a$  axis. This response to external pressure arises from (i) the highly incompressible ( $\text{CO}_3$ ) carbonate units being arranged parallel to this axis and (ii) the stacking of the aforementioned

complex sheets of Zn/Cu-centered oxygen polyhedra, arranged in such a way that the intersheets' distance is relatively incompressible despite being hydrogen bonded. The compressibility of the  $b$  and  $c$  axes is directly attributable to the compression of cation-centered polyhedra (see Figure 2). The experimental (theoretical) axial compressibilities of the HP  $P$ -1 phase are  $\kappa_{a0} = 2.13(10) \cdot 10^{-3} \text{ GPa}^{-1}$  ( $2.80(4) \cdot 10^{-3} \text{ GPa}^{-1}$ ),  $\kappa_{b0} = 3.43(14) \cdot 10^{-3} \text{ GPa}^{-1}$  ( $4.34(5) \cdot 10^{-3} \text{ GPa}^{-1}$ ) and  $\kappa_{c0} = 2.62(9) \cdot 10^{-3} \text{ GPa}^{-1}$  ( $3.00(3) \cdot 10^{-3} \text{ GPa}^{-1}$ ), evidencing the compressibility reduction in the distorted dense phase. The inset of Figure 5 shows the decrease in the monoclinic  $\beta$  angle of the  $P2_1/m$  structure, with a linear variation of  $-0.233(4)^\circ/\text{GPa}$ . At the phase transition, the  $\alpha$  and  $\gamma$  angles shift from  $90^\circ$  by  $0.28(7)^\circ$  and  $-0.48(8)^\circ$ , respectively, the former being approximately constant upon further compression and the latter decreasing continuously.

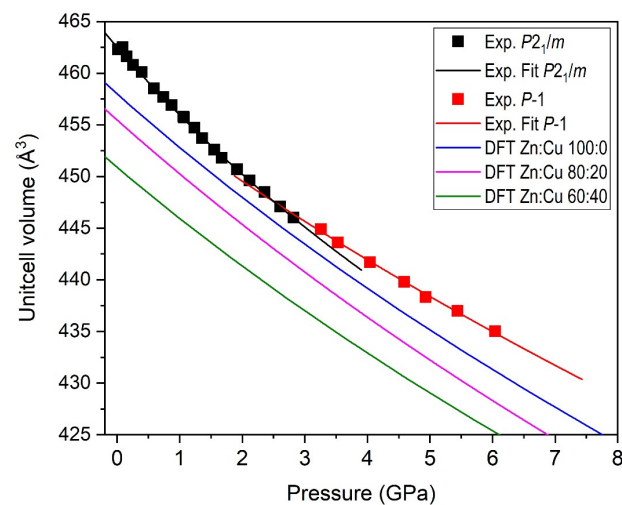


**Figure 4.** Pressure dependence of the unit-cell volume of  $\text{Zn}_{3.78(2)}\text{Cu}_{1.22(2)}(\text{CO}_3)_2(\text{OH})_6$  aurichalcite.  $P2_1/m$  and  $P$ -1 experimental data are depicted as black and red solid squares, respectively. Fits to experimental data in the pressure ranges 0–3 and 3–6 GPa are represented as solid black and red lines. DFT data for 10:0, 8:2 and 6:4 Zn:Cu ratios are represented as solid blue, magenta and green lines, respectively.

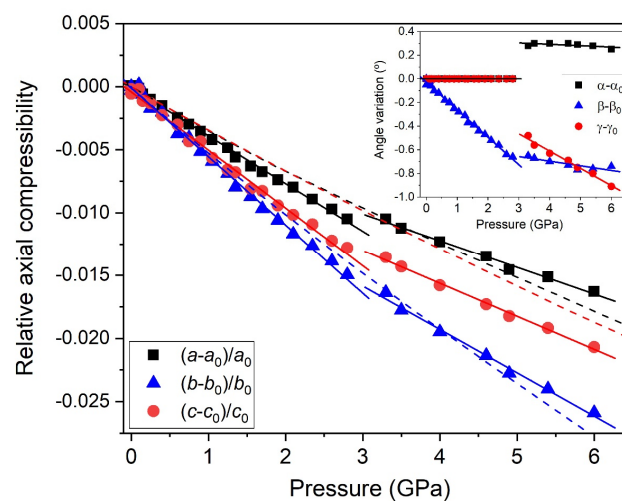


**Figure 5.** Relative axial compressibilities of the  $P2_1/m$  and  $P$ -1 aurichalcite phases. Experimental relative contractions  $(a - a_0)/a_0$ ,  $(b - b_0)/b_0$  and  $(c - c_0)/c_0$  are represented as black squares, blue triangles and red circles, respectively. Solid lines are linear fits to our experimental data. Results from DFT calculations for a Zn:Cu ratio of 8:2 are shown as dashed lines. (Inset) Unit-cell angles change upon compression.



In addition to the DFT calculations of the aurichalcite structure, we also carried out simulations of the hydrozincite structure with different Zn:Cu ratios. This structure found experimentally for the Zn end-member  $\text{Zn}_5(\text{CO}_3)_2(\text{OH})_6$  [27] has similar lattice parameters as aurichalcite; it is described with the monoclinic  $C2/m$  space group, and all the cation-centered oxygen polyhedra complex sheets are interconnected via carbonate groups, forming a three-dimensional structure (see Figure 6, to be compared with aurichalcite in Figure 2). We find that the aurichalcite structure is energetically more stable than the hydrozincite one for compositions Zn:Cu = 10:0 to 6:4 at room pressure. Aurichalcite is also more stable upon compression for Cu-bearing samples. The pure Zn aurichalcite phase, however, was predicted to transform into hydrozincite at 18 GPa (see Figure 7). This implies that the hydrozincite structure previously reported would be metastable [27].

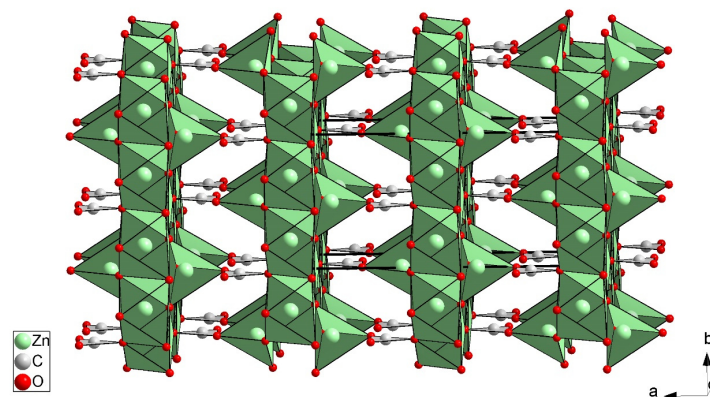


**Figure 6.** The structure of experimental  $\text{Zn}_5(\text{CO}_3)_2(\text{OH})_6$  hydrozincite reported in the literature [27] projected roughly along the (001) direction. Green, red and gray spheres correspond to the Zn, O and C atoms, respectively. Cation-centered oxygen polyhedra are depicted.

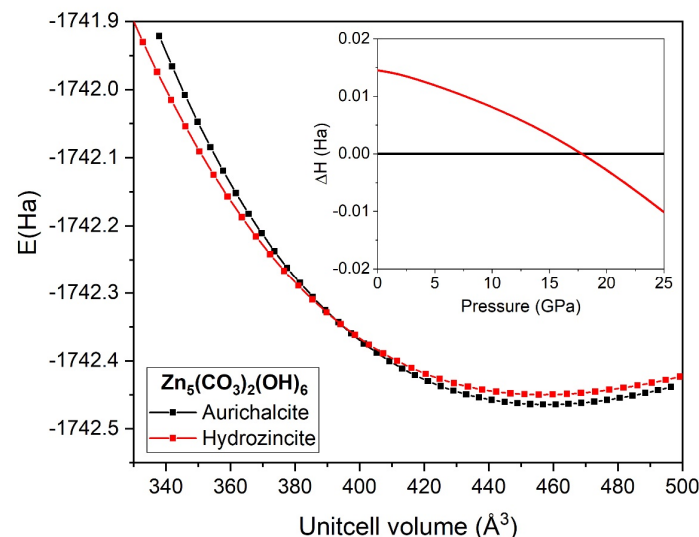


**Figure 7.** Cohesive energy as a function of the unit-cell volume for  $\text{Zn}_5(\text{CO}_3)_2(\text{OH})_6$   $P2_1/m$  aurichalcite-type [23,24] and  $C2/m$  hydrozincite-type structures [27]. Inset: Enthalpy difference as a function of pressure, showing the stability of hydrozincite with respect to aurichalcite above 18 GPa.

#### 4. Conclusions

According to the literature, the aurichalcite  $\text{Zn}_x\text{Cu}_{5-x}(\text{CO}_3)_2(\text{OH})_6$  structure has been encountered with a wide spectrum of compositions that range from  $x = 4.17$  to  $x = 2.22$  [23,24]. Diffraction and spectroscopic measurements have confirmed that Cu atoms are distributed across several metal sites of the monoclinic  $P2_1/m$  layered aurichalcite

structure, but they preferentially occupy the Jahn–Teller-elongated octahedral and trigonal bipyramidal sites, with the Zn atoms entering the more regular octahedral and tetrahedral sites [28,29]. The pure Zn end-member ( $x = 5$ ) was reported to crystallize as another monoclinic structure, S.G.  $C2/m$ , with similar lattice parameters but a three-dimensional framework [27]. Our DFT results show, however, that the aurichalcite-type structure is energetically favorable with respect to the hydrozincite-type in the compositional range  $x = 5$ –3 at ambient pressure, which suggests that the experimentally found hydrozincite phase is metastable.

The structural behavior of aurichalcite upon compression has been studied both experimentally in a natural sample with chemical composition  $Zn_{3.78(2)}Cu_{1.22(2)}(CO_3)_2(OH)_6$  and theoretically by DFT calculations on stoichiometries  $x = 5, 4$  and 3. The mineral was found to be stable up to 3 GPa, where it undergoes a second-order phase transition to a distorted triclinic  $P-1$  structure. A Murnaghan equation of state was fit to the experimental P-V data set of the initial  $P2_1/m$  aurichalcite, yielding a bulk modulus of  $B_0 = 66(2)$  GPa with a first-pressure derivative of  $B'_0 = 9(2)$ . Other basic copper and zinc carbonates such as malachite and azurite have considerably smaller bulk moduli. The relative incompressibility of the layered aurichalcite structure has mainly been related to the number of directed hydrogen bonds between carbonate groups and the cation-centered oxygen polyhedra complex sheets. Its compressibility is slightly anisotropic, with axial compressibilities  $\kappa_{a0} = 3.79(5) \cdot 10^{-3}$  GPa $^{-1}$ ,  $\kappa_{b0} = 5.44(9) \cdot 10^{-3}$  GPa $^{-1}$  and  $\kappa_{c0} = 4.61(9) \cdot 10^{-3}$  GPa $^{-1}$ , directly attributed to the directionality of hydrogen bonds along the  $a$  axis and the different cation-centered polyhedral compressibilities. Beyond the phase transition, the structure is significantly less compressible. Moreover, the DFT results evidence that both the unit-cell volume and compressibility of the aurichalcite structure increase with Zn content. Finally, our simulations show that the hydrozincite-type structure is energetically more stable than the aurichalcite-type structure above 18 GPa for the Zn end-member  $Zn_5(CO_3)_2(OH)_6$ .

**Supplementary Materials:** The following supporting information can be downloaded at <https://www.mdpi.com/article/10.3390/min13050619/s1>: Table S1: Energies and volumes per unit cell of the equilibrium geometries of the various Zn8/Cu2 atomic configurations in the aurichalcite structure, relative to the minimum-energy configuration; Table S2: Energies and volumes per unit cell of the equilibrium geometries of the various Zn8/Cu2 atomic configurations in the hydrozincite structure, relative to the minimum-energy configuration; Figure S1: Energy versus unit cell volume for the three aurichalcite and hydrozincite structures considered in this work; Figure S2: Enthalpy versus pressure for the three aurichalcite and hydrozincite structures considered in this work, relative to the enthalpy of the minimum-energy aurichalcite structure; Figure S3: Experimental XRD pattern and LeBail refinement at 5.4 GPa; Cif S1: cif file from DFT calculations for a Zn:Cu 8:2 composition at 2.76 GPa.

**Author Contributions:** Conceptualization, D.S.-P.; high-pressure XRD experiments, D.S.-P., A.O.-d.-l.-R., R.O. and C.P.; first-principle calculations, A.O.-d.-l.-R.; formal analysis, R.C.-J. and D.S.-P.; writing, R.C.-J. and D.S.-P.; review, all the authors. All authors have read and agreed to the published version of the manuscript.

**Funding:** This research was funded by the Spanish Ministerio de Ciencia e Innovación (MICINN) and the Agencia Estatal de Investigación under project PGC2021-125518NB-I00 (cofinanced by EU FEDER funds), as well as by the Generalitat Valenciana under projects CIAICO/2021/241 and MFA/2022/007 (funded by the European Union—Next Generation EU). A.O.R. acknowledges the financial support of the Spanish MINECO RyC-2016-20301 Ramón y Cajal Grant. The authors also thank the MALTA Consolider supercomputing centre and Compute Canada for computational resources and ALBA-CELLS synchrotron for providing beamtime under experiment 2022025712.

**Data Availability Statement:** The raw data required to reproduce the above findings are available from the authors upon a reasonable request.

**Acknowledgments:** Diffraction experiments were performed at the MSPD beamline with the collaboration of ALBA staff.

**Conflicts of Interest:** The authors declare no conflict of interest. The funders had no role in the design of the study; in the collection, analyses or interpretation of data; in the writing of the manuscript; or in the decision to publish the results.

## References

1. Dasgupta, R. Ingassing, storage, and outgassing of terrestrial carbon through geologic time. *Rev. Mineral. Geochem.* **2013**, *75*, 183. [[CrossRef](#)]
2. Suito, K.; Namba, J.; Horikawa, T.; Taniguchi, Y.; Sakurai, N.; Kobayashi, M.; Onodera, A.; Shimomura, O.; Kikegawa, T. Phase relations of  $\text{CaCO}_3$  at high pressure and high temperature. *Am. Mineral.* **2001**, *86*, 997–1002. [[CrossRef](#)]
3. Isshiki, M.; Irifune, T.; Hirose, K.; Ono, S.; Ohishi, Y.; Watanuki, T.; Nishibori, E.; Takata, M.; Sakata, M. Stability of magnesite and its high-pressure form in the lowermost mantle. *Nature* **2004**, *427*, 60–63. [[CrossRef](#)] [[PubMed](#)]
4. Boulard, E.; Menguy, N.; Auzende, A.; Benzerara, K.; Bureau, H.; Antonangeli, D.; Corgne, A.; Morard, G.; Siebert, J.; Perrillat, J.P. Experimental investigation of the stability of Fe-rich carbonates in the lower mantle. *J. Geophys. Res.* **2012**, *117*, B02208. [[CrossRef](#)]
5. Chulia-Jordan, R.; Santamaria-Perez, D.; Otero-de-la-Roza, A.; Ruiz-Fuertes, J.; Marqueño, T.; Gomis, O.; MacLeod, S.; Popescu, C. Phase stability of natural  $\text{Ni}_{0.75}\text{Mg}_{0.22}\text{Ca}_{0.03}\text{CO}_3$  gaspeite mineral at high pressure and temperature. *J. Phys. Chem. C* **2020**, *124*, 19781–19792. [[CrossRef](#)]
6. Zhang, J.; Reeder, R.J. Comparative compressibilities of calcite structure carbonates: Deviations from empirical relations. *Am. Mineral.* **1999**, *84*, 861–870. [[CrossRef](#)]
7. Ono, S.; Brodholt, J.P.; Price, G.D. Phase transitions of  $\text{BaCO}_3$  at high pressures. *Mineral. Mag.* **2008**, *72*, 659–665. [[CrossRef](#)]
8. Ono, S. High-pressure phase transformation in  $\text{MnCO}_3$ : A synchrotron XRD study. *Mineral. Mag.* **2007**, *71*, 105–111. [[CrossRef](#)]
9. Mao, Z.; Armentrout, M.; Rainey, E.; Manning, C.E.; Dera, P.; Prakapenka, V.B.; Kavner, A. Dolomite III: A new candidate lower mantle carbonate. *Geophys. Res. Lett.* **2011**, *38*, L22303. [[CrossRef](#)]
10. Merlini, M.; Crichton, W.A.; Hanfland, M.; Gemmi, M.; Müller, H.; Kuppenko, I.; Dubrovinsky, L. Structures of dolomite at ultrahigh pressure and their influence on the deep carbon cycle. *Proceed. Nat. Acad. Sci. USA* **2012**, *109*, 13509–13514. [[CrossRef](#)]
11. Santamaria-Perez, D.; Otero-de-la-Roza, A.; Ruiz-Fuertes, J.; Chulia-Jordan, R.; Marqueño, T.; MacLeod, S.; Popescu, C. Pressure and temperature effects on low-density  $\text{Mg}_3\text{Ca}(\text{CO}_3)_4$  huntite carbonate. *J. Phys. Chem. C* **2020**, *124*, 1077–1087. [[CrossRef](#)]
12. Chulia-Jordan, R.; Santamaria-Perez, D.; Ruiz-Fuertes, J.; Otero-de-la-Roza, A.; Popescu, C. Compressibility and phase stability of iron-rich ankerite. *Minerals* **2021**, *11*, 607. [[CrossRef](#)]
13. Chulia-Jordan, R.; Santamaria-Perez, D.; Ruiz-Fuertes, J.; Otero-de-la-Roza, A.; Popescu, C. Crystal structure of  $\text{BaCa}(\text{CO}_3)_2$  alstonite carbonate and its phase stability upon compression. *ACS Earth Space Chem.* **2021**, *5*, 1130–1139. [[CrossRef](#)]
14. Chulia-Jordan, R.; Santamaria-Perez, D.; Gonzalez-Platas, J.; Otero-de-la-Roza, A.; Ruiz-Fuertes, J.; Popescu, C. Phase stability and dense polymorph of the  $\text{BaCa}(\text{CO}_3)_2$  barytoalcite carbonate. *Sci. Rep.* **2022**, *12*, 7413. [[CrossRef](#)]
15. Gao, J.; Huang, W.F.; Wu, X.; Fan, D.W.; Wu, Z.Y.; Xia, D.G.; Qin, S. Compressibility of carbonophosphate bradleyite  $\text{Na}_3\text{Mg}(\text{CO}_3)(\text{PO}_4)$  by X-ray diffraction and Raman spectroscopy. *Phys. Chem. Miner.* **2015**, *42*, 191–201. [[CrossRef](#)]
16. Gao, J.; Wu, X.; Qin, S. The crystal chemistry and the compressibility of silicatecarbonate minerals: Spurrite, galuskinite and tilleyite. *Geosci. Front.* **2015**, *6*, 771–777. [[CrossRef](#)]
17. Santamaria-Perez, D.; Ruiz-Fuertes, J.; Marqueño, T.; Pellicer-Porres, J.; Chulia-Jordan, R.; MacLeod, S.; Popescu, C. Structural behavior of natural silicate-carbonate spurrite mineral,  $\text{Ca}_5(\text{SiO}_4)_2(\text{CO}_3)$ , under high-pressure, high-temperature conditions. *Inorg. Chem.* **2018**, *57*, 98–105. [[CrossRef](#)]
18. Santamaria-Perez, D.; Ruiz-Fuertes, J.; Peña-Alvarez, M.; Chulia-Jordan, R.; Marqueño, T.; Zimmer, D.; Gutierrez-Cano, V.; MacLeod, S.; Gregoryanz, E.; Popescu, C.; et al. Post-tilleyite, a dense calcium silicate-carbonate phase. *Sci. Rep.* **2019**, *9*, 7898. [[CrossRef](#)]
19. Merlini, M.; Perchiazzi, N.; Hanfland, M.; Bossak, A. Phase transition at high pressure in  $\text{Cu}_2\text{CO}_3(\text{OH})_2$  related to the reduction of the Jahn-Teller effect. *Acta Cryst. B* **2012**, *68*, 266–274. [[CrossRef](#)]
20. Xu, J.; Kuang, Y.; Zhang, B.; Liu, Y.; Fan, D.; Zhou, W.; Xie, H. High-pressure study of azurite  $\text{Cu}_3(\text{CO}_3)_2(\text{OH})_2$  by synchrotron radiation X-ray diffraction and Raman spectroscopy. *Phys. Chem. Miner.* **2015**, *42*, 805–816. [[CrossRef](#)]
21. Gao, J.; Yuan, X.; Chen, B.; Liu, Z.; Su, W. High-pressure phase transformation of carbonate malachite  $\text{Cu}_2(\text{CO}_3)(\text{OH})_2$  driven by  $[\text{CuO}_6]$  regularization and  $[\text{CO}_3]$  rotation. *Geosci. Front.* **2021**, *12*, 965–976. [[CrossRef](#)]
22. Gorce, J.S.; Caddick, M.J.; Bodnar, R.J. Thermodynamic constraints on carbonate stability and carbon volatility during subduction. *Earth Planet Sci. Lett.* **2019**, *519*, 213–222. [[CrossRef](#)]
23. Giester, G.; Rieck, B. Crystal structure refinement of aurichalcite,  $(\text{Cu,Zn})_5(\text{OH})_6(\text{CO}_3)_2$ , from the Lavrion Mining District, Greece. *N. Jb. Miner. Abh.* **2014**, *191*, 225–232. [[CrossRef](#)]
24. Harding, M.M.; Kariuki, B.M.; Cernik, R.; Cressey, G. The structure of Aurichalcite,  $(\text{Cu,Zn})_5(\text{OH})_6(\text{CO}_3)_2$ , determined from a microcrystal. *Acta Cryst. B* **1994**, *50*, 673–676. [[CrossRef](#)]
25. Wang, D.; Zhao, J.; Song, H.; Chou, L. Characterization and performance of  $\text{Cu/ZnO/Al}_2\text{O}_3$  catalysts prepared via decomposition of  $\text{M}(\text{Cu,Zn})$ -ammonia complexes under sub-atmospheric pressure for methanol synthesis from  $\text{H}_2$  and  $\text{CO}_2$ . *J. Nat. Gas Chem.* **2011**, *20*, 629–634. [[CrossRef](#)]

26. Charnock, J.M.; Schofield, P.F.; Henderson, C.M.B.; Cressey, G.; Cressey, B.A. Cu and Zn ordering in aurichalcite. *Mineral. Mag.* **1996**, *60*, 887–896. [[CrossRef](#)]
27. Ghose, S. The crystal structure of Hydrozincite,  $Zn_5(OH)_6(CO_3)_2$ . *Acta Cryst.* **1964**, *17*, 1051. [[CrossRef](#)]
28. Zheng, H.; Li, J.; Zhang, X.; Li, Z.; Xie, K. Structural and electronic properties of Cu-doped  $Zn_5(OH)_6(CO_3)_2$  from first principles. *J. Mater. Sci.* **2015**, *50*, 6794–6807. [[CrossRef](#)]
29. Reddy, B.J.; Nieto, F.; Sanchez-Navas, A. Spectroscopic characterization of rosasite and aurichalcite. *N. Jb. Miner. Mh.* **2004**, *7*, 302–316. [[CrossRef](#)]
30. Reddy, B.J.; Frost, R.L.; Locke, A. Synthesis and spectroscopic characterization of aurichalcite  $(Cu,Zn)_5(OH)_6(CO_3)_2$ : Implications for Cu-ZnO catalyst precursors. *Transition Met. Chem.* **2008**, *33*, 331–339. [[CrossRef](#)]
31. Frost, R.L.; Locke, A.J.; Hales, M.C.; Martens, W.N. Thermal stability and synthetic aurichalcite implications for making mixed metal oxides for use as catalysts. *J. Therm. Anal. Calor.* **2008**, *94*, 203–208. [[CrossRef](#)]
32. Fauth, F.; Peral, I.; Popescu, C.; Knapp, M. The new material science powder diffraction beamline at ALBA synchrotron. *Powder Diffr.* **2013**, *28*, S360. [[CrossRef](#)]
33. Klotz, S.; Chervin, J.C.; Munsch, P.; Le Marchand, G. Hydrostatic limits of 11 pressure transmitting media. *J. Phys. D Appl. Phys.* **2009**, *42*, 075413. [[CrossRef](#)]
34. Dewaele, A.; Loubeyre, P.; Mezouar, M. Equations of state of six metals above 94 GPa. *Phys. Rev. B.* **2004**, *70*, 094112. [[CrossRef](#)]
35. Prescher, C.; Prakapenka, V.B. DIOPTAS: A Program for Reduction of Two-Dimensional X-Ray Diffraction Data and Data Exploration. *High Press. Res.* **2015**, *35*, 223–230. [[CrossRef](#)]
36. Holland, T.J.B.; Redfern, S.A.T. Unit cell refinement from powder diffraction data: The use of regression diagnostics. *Mineral. Mag.* **1997**, *61*, 65–77. [[CrossRef](#)]
37. Rodriguez-Carvajal, J. Recent advances in magnetic structure determination by neutron powder diffraction. *Phys. B.* **1993**, *192*, 55–69. [[CrossRef](#)]
38. Nolze, G.; Kraus, W. Powdercell 2.0 for Windows. *Powd. Diffract.* **1998**, *13*, 256–259.
39. Blöchl, P.E. Projector augmented-wave method. *Phys. Rev. B.* **1994**, *50*, 17953. [[CrossRef](#)]
40. Giannozzi, P.; Andreussi, O.; Brumme, T.; Bunau, O.; Nardelli, M.B.; Calandra, M.; Car, R.; Cavazzoni, C.; Ceresoli, D.; Cococcioni, M.; et al. Advanced capabilities for materials modelling with Quantum ESPRESSO. *J. Phys. Cond. Matter.* **2017**, *29*, 465901. [[CrossRef](#)]
41. Becke, A.D. On the large-gradient behavior of the density functional exchange energy. *J. Chem. Phys.* **1986**, *85*, 7184. [[CrossRef](#)]
42. Perdew, J.P.; Burke, K.; Ernzerhof, M. Generalized Gradient Approximation Made Simple. *Phys. Rev. Lett.* **1996**, *77*, 3865–3868. [[CrossRef](#)] [[PubMed](#)]
43. Johnson, E.R. The Exchange-Hole Dipole Moment Dispersion Model. In *Non-Covalent Interactions in Quantum Chemistry and Physics*; Elsevier: Amsterdam, The Netherlands, 2017; pp. 169–194.
44. Becke, A.D.; Johnson, E.R. Exchange-hole dipole moment and the dispersion interaction revisited. *J. Chem. Phys.* **2007**, *127*, 154108. [[CrossRef](#)] [[PubMed](#)]
45. Otero-de-la-Roza, A.; Johnson, E.R. Van der Waals interactions in solids using the exchange-hole dipole moment model. *J. Chem. Phys.* **2012**, *136*, 174109. [[CrossRef](#)]
46. Borlido, P.; Aull, T.; Huran, A.W.; Tran, F.; Marques, M.A.L.; Botti, S. Large-scale benchmark of exchange-correlation functionals for the determination of electronic band gaps of solids. *J. Chem. Theory Comput.* **2019**, *15*, 5069–5079. [[CrossRef](#)]
47. Dal Corso, A. Pseudopotentials periodic table: From H to Pu. *Comput. Mater. Sci.* **2014**, *95*, 337–350. [[CrossRef](#)]
48. Marzari, N.; Vanderbilt, D.; De Vita, A.; Payne, M.C. Thermal contraction and disordering of the Al (110) surface. *Phys. Rev. Lett.* **1999**, *82*, 3296. [[CrossRef](#)]
49. Otero-de-la-Roza, A.; Luaña, V. Gibbs2: A new version of the quasi-harmonic model code. I. Robust treatment of the static data. *Comput. Phys. Commun.* **2011**, *182*, 1708–1720. [[CrossRef](#)]
50. Otero-de-la-Roza, A.; Abbasi-Perez, D.; Luaña, V. Gibbs2: A new version of the quasi-harmonic model code. II. Models for solid-state thermodynamics, features and implementation. *Comput. Phys. Commun.* **2011**, *182*, 2232–2248. [[CrossRef](#)]
51. Santamaria-Perez, D.; Pavic, L.; Chulia-Jordan, R.; Ruiz-Fuertes, J.; Popescu, C.; Otero-de-la-Roza, A. Phase stability of stress-sensitive  $Ag_2CO_3$  silver carbonate at high pressures and temperatures. *Solid State Sci.* **2023**, *135*, 107068. [[CrossRef](#)]

**Disclaimer/Publisher’s Note:** The statements, opinions and data contained in all publications are solely those of the individual author(s) and contributor(s) and not of MDPI and/or the editor(s). MDPI and/or the editor(s) disclaim responsibility for any injury to people or property resulting from any ideas, methods, instructions or products referred to in the content.